

Article

High-Power, High-Efficiency GaSb-Based Laser with Compositionally Linearly Graded AlGaAsSb Layer

Yihang Chen ^{1,2}, Chengao Yang ^{1,2,*}, Tianfang Wang ^{1,2}, Hongguang Yu ^{1,2}, Jianmei Shi ^{1,2}, Xiangbin Su ^{1,2}, Yu Zhang ^{1,2}, Youwen Zhao ^{1,2}, Cunzhu Tong ³, Donghai Wu ^{1,2}, Yingqiang Xu ^{1,2,*}, Haiqiao Ni ^{1,2} and Zhichuan Niu ^{1,2,*}

¹ State Key Laboratory for Superlattices and Microstructures, Institute of Semiconductors, Chinese Academy of Sciences, Beijing 100083, China; cheniyhang18@semi.ac.cn (Y.C.)

² Center of Materials Science and Optoelectronics Engineering, University of Chinese Academy of Sciences, Beijing 100049, China

³ Changchun Institute of Optics, Fine Mechanics and Physics, Chinese Academy of Sciences, Changchun 130033, China

* Correspondence: yangchengao@semi.ac.cn (C.Y.); yingqxu@semi.ac.cn (Y.X.); zniu@semi.ac.cn (Z.N.)

Abstract: We propose a novel graded AlGaAsSb layer growth method to achieve a super-linear interface by precisely controlling the cell temperature and valve position. Atomically smooth surface and lattice-matched epitaxy was confirmed by AFM and the HRXRD characterization of the graded AlGaAsSb layer sample. With the inserted graded layer between the cladding and waveguide layers, high-power, high-efficiency GaSb-based laser emitters and laser bars were confirmed. The linearly graded interface layer smooths the potential barrier peak between the cladding and waveguide layers, which resulted in a low turn-on voltage of 0.65 V and an ultra-low series resistance of 0.144 Ω. A maximum continuous-wave output power of 1.8 W was obtained with a high power conversion efficiency of 28% at 1.1 A and 12% at 8 A. A facet-coated laser bar was also fabricated with a record-high CW output power of 18 W. A high internal quantum efficiency of 83 was maintained at 40 °C, implying improved carrier injection efficiency, which benefits from the built-in electric field of the composition-graded AlGaAsSb layer.

Keywords: GaSb-based diode lasers; high power; molecular beam epitaxy



Citation: Chen, Y.; Yang, C.; Wang, T.; Yu, H.; Shi, J.; Su, X.; Zhang, Y.; Zhao, Y.; Tong, C.; Wu, D.; et al. High-Power, High-Efficiency GaSb-Based Laser with Compositionally Linearly Graded AlGaAsSb Layer. *Appl. Sci.* **2023**, *13*, 5506. <https://doi.org/10.3390/app13095506>

Academic Editor: John Xiupu Zhang

Received: 9 April 2023

Revised: 24 April 2023

Accepted: 25 April 2023

Published: 28 April 2023



Copyright: © 2023 by the authors. Licensee MDPI, Basel, Switzerland. This article is an open access article distributed under the terms and conditions of the Creative Commons Attribution (CC BY) license (<https://creativecommons.org/licenses/by/4.0/>).

1. Introduction

GaSb-based lasers are the most promising candidates among mid-infrared lasers owing to their high efficiency, small volume, and low cost, which are in high demand for gas detection [1], pollution monitoring [2], aesthetic surgery [3], material processing [4], and resonant pumping of the Ho-doped host [5]. Radiation recombination in InGaAsSb/AlGaAsSb type-I quantum wells offers output radiation with wavelengths covering 2–3 μm and exhibits higher efficiency and temperature stability than that in InP-based quantum wells. To achieve high output power, a broad-area ridge waveguide is the normally used structure in electrically pumped diode lasers. Benefiting from the flexibility of the energy band design and precise MBE material growth techniques, both wide wavelength coverage and room-temperature continuous-wave operation have been achieved in GaSb-based broad-area lasers.

In order to achieve high-power, high-efficiency output performance, an optimized separate confinement heterostructure (SCH) design [6], a narrow waveguide layer with an optimized doping profile [7], an asymmetric waveguide layer with a carrier barrier [8], and cascade type-I quantum wells [9] have been attempted and resulted in a low threshold, low internal loss, and Watt-level high-output-power InGaAsSb/AlGaAsSb quantum-well lasers. Except for cascade type-I quantum-well lasers, the abovementioned schemes are made of composition-fixed functional layers, which limits the design flexibility of GaSb-based lasers.

The composition-graded layer was first proposed in the GaAs/AlGaAs system, which is known as a graded-index separate confinement heterostructure (GRIN SCH) and has been well developed in InP and GaN systems [10–13]. The composition-graded layer epitaxy technique provides more flexibility for semiconductor device designs, e.g., the modification of the built-in electric field, bandgap profile, and refractive index profile [14–16]. Further improving the performance of GaSb-based lasers requires addressing the series resistance caused by the abrupt interface between the waveguide layer and cladding layer, which remains a severe problem. On the one hand, series resistance causes power dissipation, and on the other hand, it accelerates heat accumulation, which lowers efficiency. Inserting a composition-graded layer into lasers can reduce the series resistance induced by a discontinuous bandgap and enhance the built-in electric field to raise the carrier injection efficiency [17].

For GaSb-based lasers, the composition-graded AlGaAsSb layer between the high-Al-content AlGaAsSb cladding layer and low-Al-content AlGaAsSb waveguide layer is supposed to maintain the lattice constant throughout the content regulation process. Composition-graded AlGaAsSb layer preparation is impeded by the two following facts: group V element competition makes the As incorporation behavior unclear, and the lattice constant is far more composition-dependent than GaAs/AlGaAs, whose lattice constant is almost independent of Al content. This difficulty also exists in InP-based devices with an InGaAsP composition-graded layer; conventional epitaxy processes divide the composition-graded region into thin sublayers, and each sublayer is grown with lattice-matched parameters to obtain the required composition profiles. However, such composition-graded epitaxy technology is more applicable to MOCVD, where source adjustment needs less response time, while GaSb-based device epitaxy is mainly accomplished in MBE systems. Growth interruption for changing and stabilizing the cell temperature may cause residual impurity incorporation for MBE [18]. A more competitive alternative is dominating beam equivalent pressure by precisely controlling the cell temperature and valve position to implement continuous growth. A continuously graded parabolic quantum-well laser was produced with such a method in the GaAs/AlGaAs system [19,20]. Such a method has not been discussed in detail in GaSb-based systems.

In this work, we put forward a novel composition-graded AlGaAsSb layer growth method by precisely controlling the group III cell temperature and group V cell valve position. Based on the analysis of the AlGaAsSb preparation features and MBE cell characteristics, we prepared a composition-graded AlGaAsSb layer sample. AFM and HRXRD results indicate that the AlGaAsSb composition modulation difficulty is overcome, and GaSb-lattice-matched, high-quality composition-graded AlGaAsSb layer epitaxy is achieved. Lasers adopting the composition-graded layer exhibit a high output power of 1.8 W, with a maximum power conversion efficiency of 28%. A high internal quantum efficiency of 83% is also maintained even at 40 °C, and the low internal loss of 4~5 cm⁻¹ shows little temperature dependence. A bar with the same epitaxial structure realized a record-high 18 W output power. Our research provides more flexibility for GaSb-based laser design.

2. Composition-Graded AlGaAsSb Layer Epitaxy

In this work, composition-graded AlGaAsSb layers were inserted between an Al_{0.25}Ga_{0.75}As_{0.02}Sb_{0.98} waveguide layer and an Al_{0.5}Ga_{0.5}As_{0.04}Sb_{0.96} cladding layer. There is a bandgap difference of ~0.3 eV between Al_{0.25}Ga_{0.75}As_{0.02}Sb_{0.98} and Al_{0.5}Ga_{0.5}As_{0.04}Sb_{0.96}. The composition-graded AlGaAsSb layer is supposed to be beneficial to the electrical characteristics and efficiency of lasers.

According to Vegard's law [21], the AlGaAsSb lattice constant is expressed as:

$$a_{Al_xGa_{(1-x)}As_ySb_{(1-y)}} = xy a_{AlAs} + x(1-y)a_{AlSb} + (1-x)y a_{GaAs} + (1-x)(1-y)a_{GaSb} \quad (1)$$

where a_{AlAs} is 5.6611 Å, a_{AlSb} is 6.1355 Å, a_{GaAs} is 5.6533 Å, and a_{GaSb} is 6.0959 Å. Linear interpolation Equation (1) is visualized in Figure 1. A 1% Al content deviation from the GaSb-lattice-matched condition will cause a 65 ppm lattice mismatch, and the same

deviation for As content will lead to a 750 ppm lattice mismatch. A strict lattice match is unnecessary for thick-layer epitaxy. Maintaining a lattice mismatch within 1000 ppm is sufficient to effectively prevent dislocation generation. The line segment connecting $\text{Al}_{0.25}\text{Ga}_{0.75}\text{As}_{0.02}\text{Sb}_{0.98}$ and $\text{Al}_{0.5}\text{Ga}_{0.5}\text{As}_{0.04}\text{Sb}_{0.96}$ represents the ideal composition modulation process throughout composition-graded AlGaAsSb layer epitaxy, and the actual composition modulation process with a deviation within the marked acceptable region can also result in high-quality AlGaAsSb epitaxy. As Figure 1 illuminates, the Al content fluctuation is acceptable on the condition that the deviation from the designed value is less than 16%, and the As content fluctuation within 1.3% is acceptable. Therefore, precise As content control is much more essential for GaSb-lattice-matched AlGaAsSb quaternary epitaxy.

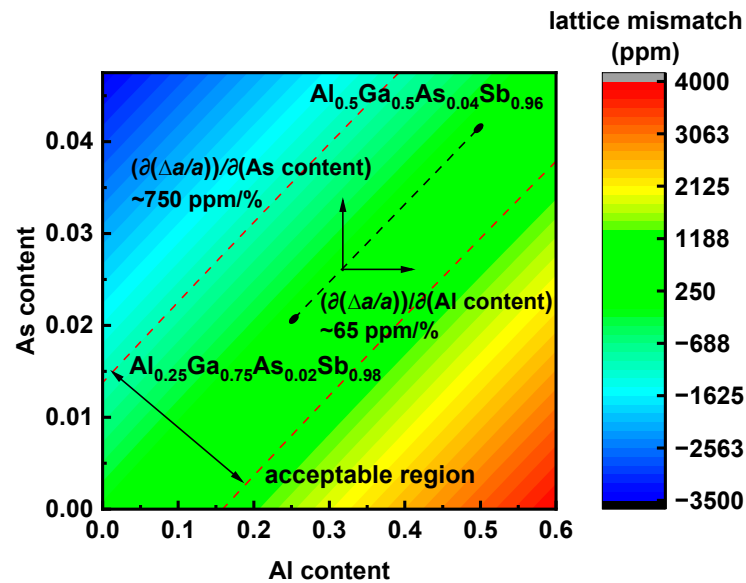


Figure 1. Dependence of lattice mismatch for Al and As contents. AlGaAsSb composition is assumed to vary along the line between $\text{Al}_{0.25}\text{Ga}_{0.75}\text{As}_{0.02}\text{Sb}_{0.98}$ and $\text{Al}_{0.5}\text{Ga}_{0.5}\text{As}_{0.04}\text{Sb}_{0.96}$. Fluctuation within the dotted line is acceptable for GaSb-lattice-matching epitaxy.

While group III elements with unit sticking coefficients are capable of being directly compositionally modified by adjusting the growth rate, the control of group V element incorporation is more complicated. Materials grown by MBE are usually in group V overpressure conditions, which means that group V elements are in excess of the available surface group V vacancies, causing their sticking coefficients to be less than one unit. The consequent group V competition for incorporation in mixed-anion semiconductor alloys causes difficulty in group V content control [22]. Considering that group V element incorporation is sensitive to group V flux and growth temperature, we kept the growth temperature, group III flux, and Sb flux constant and vary the As cell valve position to determine the GaSb-lattice-matched AlGaAsSb epitaxy condition in the following experiment.

A linear relationship between the As content of AlGaAsSb and the As beam equivalent pressure (BEP) in low-As-content conditions has been reported [23]. An experiment was conducted to determine the As BEP dependence of As content in our equipment. The substrate temperature was calibrated by the $2 \times 5 \rightarrow 1 \times 3$ reconstruction transition of the GaSb surface, which is set as T_c , according to RHEED observations, and the growth temperature is 130°C above T_c for high-quality AlGaAsSb epitaxy. The lattice mismatch was experimentally deduced from the HRXRD diffraction peak position difference of the epitaxial layer and substrate, according to Equation (2) [24].

$$\frac{\Delta a}{a} = (\theta_s - \theta_e) \cot \theta_s \quad (2)$$

where θ_s is the diffraction angle of the substrate, and θ_e is the diffraction angle of the epitaxial layer.

Figure 2 shows how the As BEP influences As incorporation when the Al and Ga growth rates are both 0.5 ML/s. When the As BEP varies from 1.40×10^{-7} hPa to 1.67×10^{-7} hPa, the lattice mismatch is maintained within ± 500 ppm. A quasi-linear dependence of As content on the As BEP is observed, and the slope is about $0.0045/1 - 10^8$ hPa, which reveals a constant As stacking coefficient within the researched As BEP range. The experiment was conducted under Sb overpressure (1.33×10^{-6} hPa), where Sb BEP has little influence on the As content and group III composition does not enhance As incorporation [25]. Therefore, it is reasonable to assume a constant As stacking coefficient throughout the composition-graded AlGaAsSb layer epitaxy process.

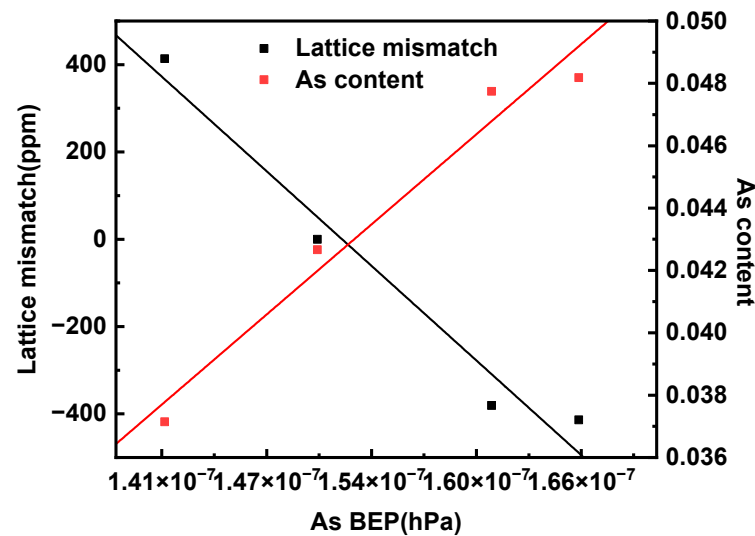


Figure 2. Influence of As BEP on As content and lattice mismatch (dots: measured; lines: fitted). A quasi-linear dependence of As BEP on As incorporation is observed, indicating a constant stacking coefficient under Sb overpressure and fixed growth temperature.

Valved cracker cells overcome the flux instability by providing a large reservoir of group V element vapor and controlling the flux with a needle valve. Real-time As flux monitoring and feedback control have been demonstrated by taking advantage of the rapid and repeatable flux response to the valve position [26]. In group V element composition-varying conditions, a step-like flux sequence is usually adopted to obtain the designed composition profile [27]. In this work, As BEP quasi-linear variation was accomplished by ramping the As cracker valve position to prevent background impurity incorporation induced by growth interruption. The As BEP is monitored by an ion gauge installed in the growth chamber. Figure 3 illustrates the As BEP profile obtained by ramping up the As valve position. The As BEP's linearly ascending segment lasts for ~ 830 s, corresponding to the valve position ramp-up procedure. The valve position is fixed after the As BEP reaches the setpoint, and the As BEP is maintained for subsequent high-Al-content AlGaAsSb epitaxy. According to Figure 2, an 800 ppm lattice mismatch is the outcome of a 2.67×10^{-8} hPa As BEP deviation. Since an As BEP deviation within 2.67×10^{-8} hPa is acceptable for lattice-matched epitaxy, the demonstrated As BEP profile can be considered a linear modulation procedure, which is functional for composition-graded AlGaAsSb layer epitaxy.

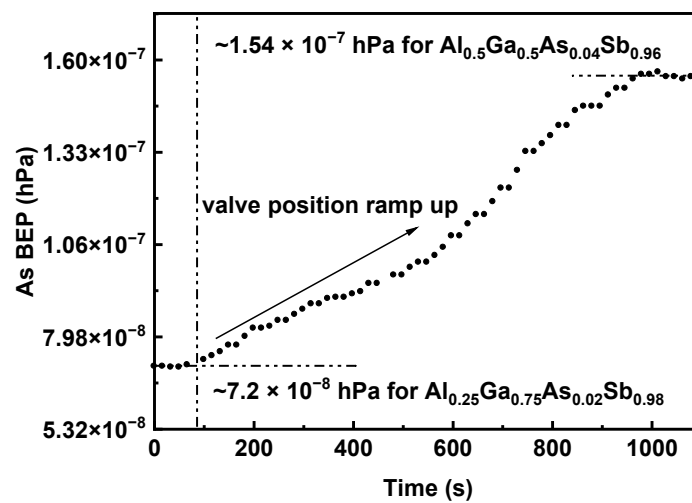


Figure 3. As BEP response to As valve position ramp-up. As valve position ramps up from $\text{Al}_{0.25}\text{Ga}_{0.75}\text{As}_{0.02}\text{Sb}_{0.98}$ growth condition to $\text{Al}_{0.5}\text{Ga}_{0.5}\text{As}_{0.04}\text{Sb}_{0.96}$ growth condition, and As BEP exhibits quasi-linear increase. As BEP settles in $\text{Al}_{0.5}\text{Ga}_{0.5}\text{As}_{0.04}\text{Sb}_{0.96}$ growth condition when As valve position reaches its destination.

Group III element diffusion cells show different operating characteristics from group V valved cracker cells: the group III element flux is directly produced by metal evaporation, which causes an exponential flux–temperature dependence in the steady-state case, and flux transients occur when the cell operating condition changes. In addition, cell temperature ramping is not as rapid as valve position ramping. However, Rouel demonstrated linear Ga growth rate modulation with a rate of change of $12.4 \text{ (\AA/h)}/\text{s}$ by linearly ramping the Ga cell temperature [28], indicating that the linear modification of group III BEP is feasible by adopting a sufficiently slow ramping rate. A similar approach was taken in our experiment, and Figure 4 shows the flux obtained in the Al temperature time-varying growth. The Al cell temperature ramp-up procedure lasts for $\sim 830 \text{ s}$, and the cell temperatures of the starting and finishing points are calibrated in advance from the RHEED oscillation curve for the specified Al growth rate, namely, 0.16 ML/s for $\text{Al}_{0.25}\text{Ga}_{0.75}\text{As}_{0.02}\text{Sb}_{0.98}$ and 0.5 ML/s for $\text{Al}_{0.5}\text{Ga}_{0.5}\text{As}_{0.04}\text{Sb}_{0.96}$. Linear Al flux modulation followed by flux fluctuation as the cell temperature reaches the setpoint is observed. Therefore, the Al shutter should be closed as soon as the composition-graded layer growth is over to avoid the influence of an Al temperature overshoot, and an interruption is necessary for temperature stabilization.

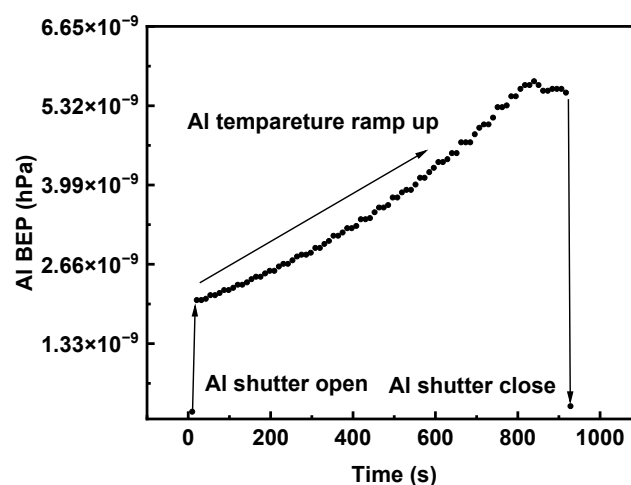


Figure 4. Al BEP response to Al temperature ramp-up. Al growth rate is linearly modified by ramping up Al cell temperature. In-time shutter closure is necessary to prevent composition fluctuation caused by temperature overshoot.

Based on the abovementioned linear Al and As flux modulation experiment, we can estimate the thickness of the composition-graded layer by using Equation (3). The Al growth rate is assumed to vary linearly with time, and GaSb-lattice-matched growth is guaranteed by As BEP modulation.

$$d = A \int_0^T (v_{Ga} + v_{Al}) dt = A \int_0^T (v_{Ga} + at + v_{Al0}) dt = AT(v_{Ga} + v_{Al0}) + \frac{aAT^2}{2} \quad (3)$$

where d is the thickness of the composition-graded layer, T is the duration of the growth process, A is a constant depending on the lattice of the GaSb substrate, and a is the ramp rate of the Al growth rate. In our linear Al modulation experiment, a was set to $4.4 \text{ (\AA/h)}/s$ to obtain quasi-equilibrium growth. A thickness of 210 nm and a growth duration of 827 s can be obtained, according to Equation (3), when the Ga growth rate is set to 0.5 ML/s and the Al growth rate ramps from 0.16 ML/s to 0.5 ML/s.

A composition-graded layer sample was grown by adopting linear As and Al BEP modification parameters. The sample consisted of a 210 nm composition-graded AlGaAsSb layer and a 10 nm GaSb cap layer. The Al content varied linearly from 0.25 to 0.5 in the composition-graded layer. The sample was characterized by AFM and HRXRD, the results are illustrated in Figure 5. In the $10 \mu\text{m} \times 10 \mu\text{m}$ AFM scanning result, clear atomic steps and 1.7 \AA RMS surface roughness indicate high epitaxial quality. A single sharp HRXRD peak implies lattice-matching growth. Similar procedures were adopted to verify the $\text{Al}_{0.5}\text{Ga}_{0.5}\text{As}_{0.04}\text{Sb}_{0.96}$ to $\text{Al}_{0.25}\text{Ga}_{0.75}\text{As}_{0.02}\text{Sb}_{0.98}$ composition-graded layer. The AFM and HRXRD results also suggest high-quality and GaSb-lattice-matching growth.

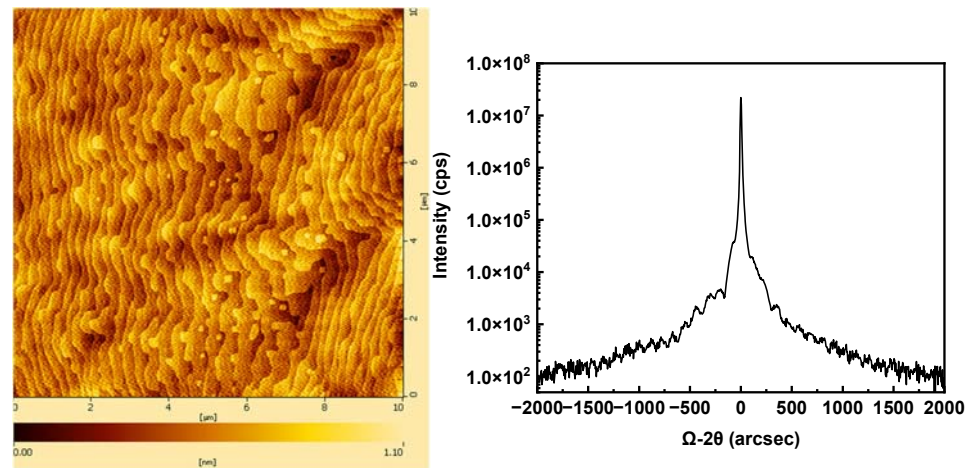


Figure 5. AFM and HRXRD results of composition-graded layer show high-quality and lattice-matched growth of composition-graded AlGaAsSb layer.

3. Laser Performance

The verified composition-graded layer was then applied to InGaSb/AlGaAsSb quantum-well lasers. As Figure 6 shows, the laser consists of a 1500 nm $\text{Al}_{0.5}\text{Ga}_{0.5}\text{As}_{0.04}\text{Sb}_{0.96}$: Te bottom cladding layer, a 210 nm $\text{Al}_{0.5}\text{Ga}_{0.5}\text{As}_{0.04}\text{Sb}_{0.96}$ to $\text{Al}_{0.25}\text{Ga}_{0.75}\text{As}_{0.02}\text{Sb}_{0.98}$ bottom composition-graded layer, a 270 nm $\text{Al}_{0.25}\text{Ga}_{0.75}\text{As}_{0.02}\text{Sb}_{0.98}$ bottom waveguide layer, a 40 nm active region, a 270 nm $\text{Al}_{0.25}\text{Ga}_{0.75}\text{As}_{0.02}\text{Sb}_{0.98}$ top waveguide layer, a 210 nm $\text{Al}_{0.25}\text{Ga}_{0.75}\text{As}_{0.02}\text{Sb}_{0.98}$ to $\text{Al}_{0.5}\text{Ga}_{0.5}\text{As}_{0.04}\text{Sb}_{0.96}$ top composition-graded layer, a 2000 nm $\text{Al}_{0.5}\text{Ga}_{0.5}\text{As}_{0.04}\text{Sb}_{0.96}$: Be top cladding layer, and a 250 nm GaSb: Be contact layer. The active region includes two 10 nm $\text{In}_{0.2}\text{Ga}_{0.8}\text{Sb}$ quantum wells, which are separated by a 20 nm $\text{Al}_{0.25}\text{Ga}_{0.75}\text{As}_{0.02}\text{Sb}_{0.98}$ barrier.

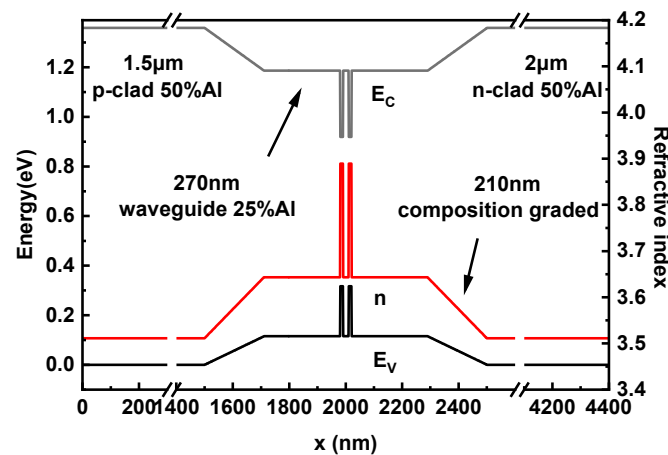


Figure 6. Energy band diagram and refractive index profile of InGaSb/AlGaAsSb diode lasers.

GaSb-lattice-matched AlGaAsSb transforms from a direct bandgap semiconductor to an indirect bandgap semiconductor when the Al content is higher than 0.45. Electrons injected from the $\text{Al}_{0.5}\text{Ga}_{0.5}\text{As}_{0.04}\text{Sb}_{0.96}$ cladding layer first localize in the X valley and are then scattered into the Γ valley while being transported through the composition-graded AlGaAsSb layer, which is smoother than electrons crossing the abrupt $\text{Al}_{0.5}\text{Ga}_{0.5}\text{As}_{0.04}\text{Sb}_{0.96}/\text{Al}_{0.25}\text{Ga}_{0.75}\text{As}_{0.02}\text{Sb}_{0.98}$ interface. In addition, composition-graded AlGaAsSb layers flatten the potential barrier peak of the heterostructure, lower the series resistance, and suppress the rectification effect caused by the potential barrier peak.

A 200 μm wide ridge pattern was prepared via the photolithography process and then etched 2 μm deep in an inductively coupled plasma reactive-ion etching (ICP-RIE) system. A 250 nm thick SiO_2 insulation layer was deposited on the ridge waveguide by plasma-enhanced chemical vapor deposition (PECVD), through which a 190 μm wide current injection window was etched by reactive-ion etching (RIE). The GaSb substrate was then thinned and polished to 120 μm thickness to reduce the series resistance. AuGeNi/Au and TiPtAu were sputtered as N contact metal and P contact metal, respectively. After the deposition of AuGeNi/Au, rapid thermal processing (RTP) was conducted to form Ohmic contact. A wafer was then cleaved into bars with different cavity lengths for subsequent experiments. Single emitters were p-side-down c-mounted on a copper heatsink with In solder, while bar lasers were mounted onto a microchannel heatsink for better heat dissipation performance. The tests were all conducted in CW or QCW (with a pulse duration of 100 μs at a 100 Hz repetition rate) operation.

For CW output performance characterization, bars with 1 mm cavity length were 5% anti-reflection- and 95% high-reflection-coated and then cleaved into 500 μm wide chips as single emitters. The CW performance at 15 $^\circ\text{C}$ of a single emitter is shown in Figure 7. The turn-on voltage is 0.65 V. Since the wavelength of our laser is 2006 nm, the theoretical lowest turn-on voltage for population inversion is the quasi-Fermi energy difference corresponding to the lasing transition, which can be expressed as Equation (4) [27]:

$$V_F = \frac{ch}{\lambda e} \approx 0.62 \text{ V} \quad (4)$$

The difference between the turn-on voltage and this theoretical lowest value is the voltage penalty induced by heterojunction barriers [29]. The low turn-on voltage demonstrates that the adoption of the composition-graded AlGaAsSb layer effectively reduces the voltage penalty and improves the performance of GaSb-based lasers. The threshold current is 230 mA, corresponding to a threshold current density of 121 A/cm^2 . Excellent threshold parameters, e.g., a low turn-on voltage and a low threshold current density, ensure the high-efficiency operation of our lasers.

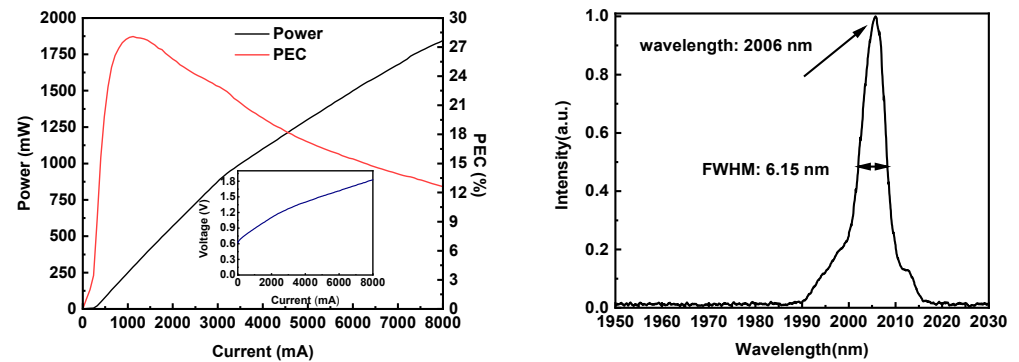


Figure 7. CW PIV characteristic of laser with 1 mm cavity length and 200 μm wide ridge measured at 15 $^{\circ}\text{C}$. High output power of 1.8 W and high maximum PCE of 28% is obtained. Wavelength and FWHM of laser operating at 3 A are 2006 nm and 6.15 nm, respectively.

The potential barrier peak of the $\text{Al}_{0.5}\text{Ga}_{0.5}\text{As}_{0.04}\text{Sb}_{0.96}/\text{Al}_{0.25}\text{Ga}_{0.75}\text{As}_{0.02}\text{Sb}_{0.98}$ heterojunction is flattened after the introduction of the composition-graded AlGaAsSb layer, and a low series resistance of 0.144 Ω is obtained. The slope efficiency decreases from ~ 0.32 W/A with the increasing operation current, which is caused by heat accumulation in the active region when lasers are characterized in CW operation. As the actual temperature of the active region rises, the threshold current for lasing rises and the internal quantum efficiency is reduced, resulting in a low power conversion efficiency [30]. Due to the optimized mounting process, the heat generated in the lasers is dispersed quickly, ensuring a high slope efficiency in a wide operating current range and delaying output power saturation caused by thermal rollover. As a result, a high output power of 1.8 W is achieved at 8 A, while a high PCE of 28% is obtained at 1.1 A. Though PCE decreases with a higher current, it remains more than 12% at 8 A. The wavelength and FWHM of the laser operating at 3 A are 2006 nm and 6.15 nm, respectively, since no additional longitudinal mode selection structure is adopted in our FP laser.

A 0.95 cm laser bar containing 19,500 μm wide emitters was 5% anti-reflection- and 95% high-reflection-coated and then mounted on a microchannel heatsink. Since the emitters in the laser bar are in parallel, the laser bar exhibits low-voltage, high-current, and high-power output performance. Nineteen emitters operating in parallel generate massive heat, and the heat distribution causes horizontal and perpendicular thermal stress in the laser bar and a consequent “smile” [31]. A microchannel heatsink with low thermal resistance and high heat flux is utilized to relieve heat accumulation and thermal stress. The laser bar with a 40% fill factor is characterized in CW operation at 15 $^{\circ}\text{C}$. The CW performance is plotted in Figure 8. A record-high CW output power of 18 W is achieved at 75 A.

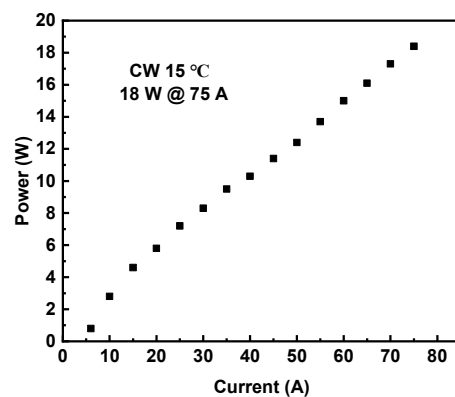


Figure 8. CW performance of 0.95 cm laser bar with 40% fill factor measured at 15 $^{\circ}\text{C}$. High output power of 18 W is obtained at 75 A.

As expressed in Equation (5) [32], internal loss and internal quantum efficiency were determined with 1 mm, 1.5 mm, and 2 mm long uncoated lasers.

$$\frac{1}{\eta_d} = \frac{q}{\hbar\omega\eta_i} \left(1 + \frac{\alpha_i}{\ln\left(\frac{1}{R_1R_2}\right)} 2L \right) \tag{5}$$

where η_d is the total slope efficiency, which is 2 times the slope efficiency measured from a single facet, q is the electric charge of a single electron, $\hbar\omega$ is the energy of a single emitted photon, α_i is the internal loss of the laser, L is the cavity length of the laser, and R_1 and R_2 are the reflectivity of each facet, which is $\sim 35\%$ for uncoated GaSb-based lasers. In order to eliminate the interference of heat accumulation with the laser efficiency, the characterization of emitters was conducted in QCW operation, and η_d was calculated according to the linear interval of the power–current relation near the lasing threshold.

The linear dependence of $1/\eta_d$ and cavity length is illustrated in Figure 9. The intercept of the linear fitted line is proportional to the internal quantum efficiency, and the internal loss can be deduced from the slope of the fitted line. With higher carrier injection efficiency benefiting from the built-in electric field of the composition-graded AlGaAsSb layer, the lasers exhibit 83% internal quantum efficiency and 3.9 cm^{-1} internal loss even at $40\text{ }^\circ\text{C}$. A low and almost temperature-independent internal loss of $4\sim 5\text{ cm}^{-1}$ is observed as the heatsink temperature rises from $5\text{ }^\circ\text{C}$ to $45\text{ }^\circ\text{C}$, which indicates that free carrier absorption is effectively reduced in our lasers. A 270 nm thick $\text{Al}_{0.25}\text{Ga}_{0.75}\text{As}_{0.02}\text{Sb}_{0.98}$ waveguide layer and a 210 nm thick composition-graded AlGaAsSb layer on both sides of the active region lower the optical confinement factor of cladding layers. The temperature insensitivity of internal loss also suggests low free carrier absorption at a higher current injection level, which maintains high efficiency at a high operation current.

The characteristic temperatures T_0 and T_1 , signifying the exponential temperature dependence of the threshold current and efficiency, are determined by using the following expressions [33]:

$$\ln I_{th}(T) = \frac{1}{T_0} \times T + \ln I_{th0} \tag{6}$$

$$\ln \eta_d(T) = -\frac{1}{T_1} \times T + \ln \eta_{d0} \tag{7}$$

where I_{th0} and η_{d0} are the ideal threshold current and slope efficiency at 0 K.

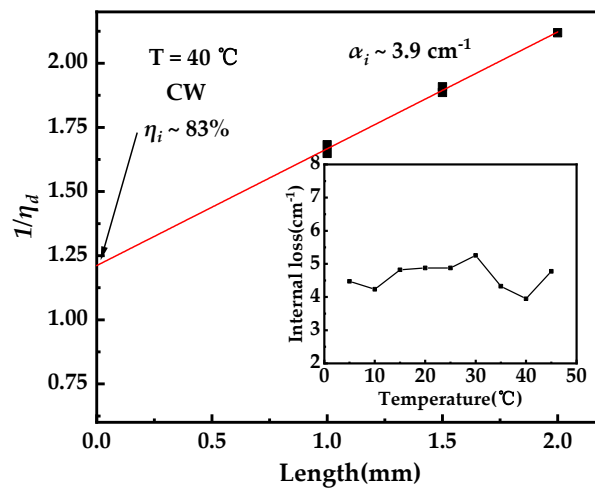


Figure 9. Values of $1/\eta_d$ with different cavity lengths. When lasers are in CW operation at $40\text{ }^\circ\text{C}$, the calculated internal efficiency assuming a cavity length approaching 0 is as high as 83%, and the internal loss is $\sim 3.9\text{ cm}^{-1}$. Internal losses are maintained within $4\sim 5\text{ cm}^{-1}$ when the heatsink temperature ranges from $5\text{ }^\circ\text{C}$ to $45\text{ }^\circ\text{C}$.

An uncoated single emitter with a 3 mm cavity length was c-mounted on a copper heatsink for power–current performance characterization. The heatsink temperature was controlled and varied from 5 °C to 45 °C with a thermoelectric cooler (TEC). The data used for the threshold current and slope efficiency calculations were extracted from the linear interval of the power–current relation near the lasing threshold to minimize the error induced by active region heating. Figure 10 plots the temperature dependence of $\ln I_{th}$ and $\ln \eta_d$ when lasers were characterized in CW operation. T_0 and T_1 deduced from the slopes of linear fitted lines are ~61 K and ~213 K, respectively, while T_0 and T_1 deduced in QCW operation are ~67 K and ~224 K, respectively. The increase in the characteristic temperature is the consequence of heat removal, and an even higher characteristic temperature is expected when the experiment is conducted in PW operation. Sufficient carrier confinement to hinder carrier leakage caused by thermal carrier emission is essential for high-efficiency laser operation, and a high characteristic temperature confirms our design is an efficient structure.

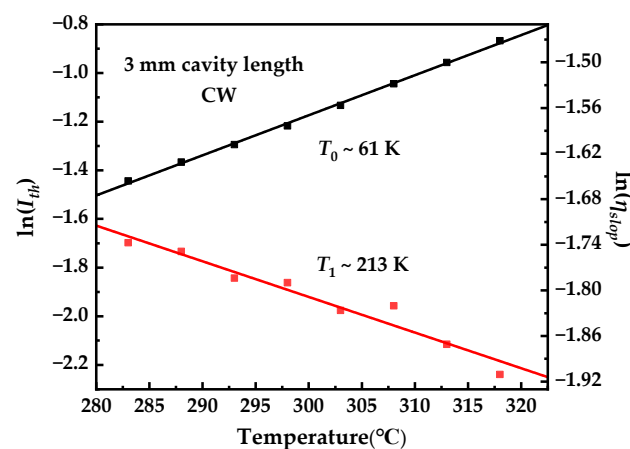


Figure 10. Characteristic temperature of laser with 3 mm long cavity in CW. Threshold current and slope efficiency are measured with 5 °C to 45 °C heatsink temperature to determine T_0 and T_1 .

4. Conclusions

In this article, we calculate the composition dependence on the AlGaAsSb lattice constant. Precise control of As incorporation is essential for GaSb-lattice-matched AlGaAsSb layer epitaxy. The linear relationship between the As BEP and As content implies a constant As stacking coefficient. The linear modulation of As and Al BEP via cell temperature and valve position ramping is demonstrated. Composition-graded AlGaAsSb layer epitaxy was implemented by adopting the BEP modulation technique, and AFM and HRXRD results suggest high-quality and GaSb-lattice-matching crystal epitaxy.

InGaSb/AlGaAsSb diode lasers with a composition-graded AlGaAsSb layer inserted between an $\text{Al}_{0.25}\text{Ga}_{0.75}\text{As}_{0.02}\text{Sb}_{0.98}$ waveguide layer and an $\text{Al}_{0.5}\text{Ga}_{0.5}\text{As}_{0.04}\text{Sb}_{0.96}$ cladding layer exhibit high-power and high-efficiency performance. A low turn-on voltage of 0.65 V and a low series resistance of 0.144 Ω were realized. A maximum output power of 1.8 W and maximum power conversion efficiency of 28% were realized at 8 A and 1.1 A, respectively. A high internal quantum efficiency of 83% and low internal loss of 3.9 cm^{-1} were measured at a 40 °C operating temperature, and 67 K T_0 and 224 K T_1 were obtained near room temperature with a 100 μs pulse duration and 100 Hz repetition rate. A 0.95 cm laser bar with the same epitaxial structure was prepared, and a high CW power of 18 W was obtained at 75 A.

Author Contributions: Conceptualization, Y.C. and C.Y.; data curation, Y.C.; funding acquisition, C.Y., H.N., Y.Z. (Youwen Zhao), C.T., D.W. and Z.N.; investigation, Y.C., T.W., H.Y., J.S. and X.S.; methodology, Y.C.; project administration, Y.Z. (Yu Zhang) and Z.N.; supervision, Z.N.; writing—original draft, Y.C.; writing—review and editing, C.Y. and Y.X. All authors have read and agreed to the published version of the manuscript.

Funding: This research was funded by the project “Announce the list and take charge” of the Major Special Plan of Science and Technology in Shanxi Province under grant number 202201030201009, the National Natural Science Foundation of China under grant number 62204238, the Jincheng Key Research and Development Project under grant number 20210209, the Chinese Academy of Sciences and Changchun City Science and Technology Innovation Cooperation Project under grant number 21SH06, the Key R&D Program of Shanxi Province under grant number 202102030201004, and the R&D Program of Guangdong Province under grant numbers 2020B0303020001 and 2018B030329001.

Institutional Review Board Statement: Not applicable.

Informed Consent Statement: Not applicable.

Data Availability Statement: The data presented in this study are available on request from the corresponding author.

Conflicts of Interest: The authors declare no conflict of interest.

References

- Jahjah, M.; Vicet, A.; Rouillard, Y. A QEPAS based methane sensor with a 2.35 μm antimonide laser. *Appl. Phys. B-Lasers Opt.* **2012**, *106*, 483–489. [[CrossRef](#)]
- Willer, U.; Saraji, M.; Khorsandi, A.; Geiser, P.; Schade, W. Near- and mid-infrared laser monitoring of industrial processes, environment and security applications. *Opt. Lasers Eng.* **2006**, *44*, 699–710. [[CrossRef](#)]
- Jean, B.; Bende, T. Mid-IR laser applications in medicine. In *Solid-State Mid-Infrared Laser Sources*; Sorokina, I.T., Vodopyanov, K.L., Eds.; Springer International Publishing AG: Gewerbestrasse, Switzerland, 2003; Volume 89, pp. 511–544.
- Ji, E.C.; Yao, Y.; Huang, Y.J.; Lu, S.; Lue, Q.T. Air-cooling 60 W Tm: Fiber laser and its applications on transparent plastics processing. In Proceedings of the Tenth International Conference on Information Optics and Photonics, Beijing, China, 8–11 July 2018.
- Li, R.; Li, J.; Shterengas, L.; Jackson, S.D. Highly efficient holmium fiber laser diode pumped at 1.94 μm . *Electron. Lett.* **2011**, *47*, 1089–1090. [[CrossRef](#)]
- Garbuzov, D.Z.; Martinelli, R.U.; Lee, H.; York, P.K.; Menna, R.J.; Connolly, J.C.; Narayan, S.Y. Ultralow loss broadened-waveguide high-power 2 μm AlGaAsSb-InGaAsSb GaSb separate-confinement quantum well lasers. *Appl. Phys. Lett.* **1996**, *69*, 2006–2008. [[CrossRef](#)]
- Rattunde, M.; Schmitz, J.; Kaufel, G.; Kelemen, M.; Weber, J.; Wagner, J. GaSb-based 2.X μm quantum-well diode lasers with low beam divergence and high output power. *Appl. Phys. Lett.* **2006**, *88*, 081115. [[CrossRef](#)]
- Chen, J.F.; Kipshidze, G.; Shterengas, L. Diode lasers with asymmetric waveguide and improved beam properties. *Appl. Phys. Lett.* **2010**, *96*, 241111. [[CrossRef](#)]
- Hosoda, T.; Feng, T.; Shterengas, L.; Kipshidze, G.; Belenky, G. High power cascade diode lasers emitting near 2 μm . *Appl. Phys. Lett.* **2016**, *108*, 131109. [[CrossRef](#)]
- Pan, W.; Wang, L.; Zhang, Y.; Lei, W.; Wang, S. MBE growth strategy and optimization of GaAsBi quantum well light emitting structure beyond 1.2 μm . *Appl. Phys. Lett.* **2019**, *114*, 152102. [[CrossRef](#)]
- Ke, C.; Li, X.; Xi, Y.; Yu, Y. Design optimization for 25 Gbit/s DML InGaAlAs/InGaAsP/InP SL-MQW laser diode incorporating temperature effect. *Opt. Commun.* **2017**, *403*, 34–40. [[CrossRef](#)]
- Chen, T.P.; Chen, W.H.; Lee, C.J.; Chu, K.Y.; Chen, L.Y.; Hung, C.W.; Tsai, T.H.; Cheng, S.Y.; Liu, W.C. Temperature-dependent characteristics of an InP/InGaAs double heterojunction bipolar transistor with a step-graded InAlGaAs collector. *J. Appl. Phys.* **2008**, *103*, 114506. [[CrossRef](#)]
- Zhang, H.; Huang, C.; Song, K.; Yu, H.; Xing, C.; Wang, D.; Liu, Z.; Sun, H. Compositionally graded III-nitride alloys: Building blocks for efficient ultraviolet optoelectronics and power electronics. *Rep. Prog. Phys.* **2021**, *84*, 044401. [[CrossRef](#)]
- Kashio, N.; Hoshi, T.; Kurishima, K.; Ida, M.; Matsuzaki, H. Composition- and doping-graded-base InP/InGaAsSb double heterojunction bipolar transistors exhibiting simultaneous $f(t)$ and $f(\text{max})$ of over 500 GHz. *IEEE Electron Device Lett.* **2014**, *35*, 1209–1211. [[CrossRef](#)]
- Hosseini, M.; Kaatuzian, H.; Taghavi, I. Graded index separate confinement heterostructure transistor laser: Analysis of various confinement structures. *Chin. Opt. Lett.* **2017**, *15*, 92–96.
- Gacevic, Z.; Vukmirovic, N. Effective refractive-index approximation: A link between structural and optical disorder of planar resonant optical structures. *Phys. Rev. Appl.* **2018**, *9*, 064041. [[CrossRef](#)]
- Hirayama, H.; Miyake, Y.; Asada, M. Analysis of current injection efficiency of separate-confinement-heterostructure quantum-film lasers. *IEEE J. Quantum Electron.* **1992**, *28*, 68–74. [[CrossRef](#)]

18. Simmonds, P.J.; Beere, H.E.; Ritchie, D.A.; Holmes, S.N. Growth-temperature optimization for low-carrier-density In_{0.75}Ga_{0.25}As-based high electron mobility transistors on InP. *J. Appl. Phys.* **2007**, *102*, 083518. [[CrossRef](#)]
19. Deimert, C.; Wasilewski, Z.R. MBE growth of continuously-graded parabolic quantum well arrays in AlGaAs. *J. Cryst. Growth* **2019**, *514*, 103–108. [[CrossRef](#)]
20. Deimert, C.; Wasilewski, Z.R. Precise control of time-varying effusion cell flux in molecular beam epitaxy. *J. Vac. Sci. Technol. A* **2021**, *39*, 043407. [[CrossRef](#)]
21. Vegard, L. The constitution of the mixed crystals and the filling of space of the atoms. *Z. Phys.* **1921**, *5*, 17–26. [[CrossRef](#)]
22. Millunchick, J.M.; Anderson, E.M.; Pearson, C.; Sarney, W.L.; Svensson, S.P. Incorporation kinetics in mixed anion compound semiconductor alloys. *J. Appl. Phys.* **2014**, *114*, 234907. [[CrossRef](#)]
23. Simanowski, S.; Walther, M.; Schmitz, J.; Kiefer, R.; Herres, N.; Fuchs, F.; Maier, M.; Mermelstein, C.; Wagner, J.; Weimann, G. Arsenic incorporation in molecular beam epitaxy (MBE) grown (AlGaIn)(AsSb) layers for 2.0–2.5 μm laser structures on GaSb substrates. *J. Cryst. Growth* **1999**, *201*, 849–853. [[CrossRef](#)]
24. Bartels, W.J. Characterization of thin layers on perfect crystals with a multipurpose high resolution X-ray diffractometer. *J. Vac. Sci. Technol. B* **1983**, *1*, 338–345. [[CrossRef](#)]
25. Selvig, E.; Fimland, B.O.; Skauli, T.; Haakenaasen, R. Calibration of the arsenic mole fraction in MBE grown GaAs_ySb_{1-y} and Al_xGa_{1-x}As_ySb_{1-y} ($y < 0.2$). *J. Cryst. Growth* **2001**, *227*, 562–565.
26. Mattord, T.J.; Sadra, K.; Srinivasan, A.; Tang, A.; Block, T.R.; Shih, Y.C.A.; Neikirk, D.P.; Streetman, B.G. Real-time flux monitoring and feedback control of a valved arsenic source. *J. Vac. Sci. Technol. B* **1993**, *11*, 1050–1052. [[CrossRef](#)]
27. Tomasulo, S.; Simon, J.; Simmonds, P.J.; Biagiotti, J.; Lee, M.L. Molecular beam epitaxy of metamorphic In_yGa_{1-y}P solar cells on mixed anion GaAs_xP_{1-x}/GaAs graded buffers. *J. Vac. Sci. Technol. B* **2011**, *29*, 03C118. [[CrossRef](#)]
28. Fernandez, R.; Harwit, A.; Kinell, D. Accurate measurements of transients and intentional rates of change in molecular beam epitaxy growth rate calibrations. *J. Vac. Sci. Technol. B* **1994**, *12*, 1023–1025. [[CrossRef](#)]
29. Mermelstein, C.; Bour, D.P.; Goodnough, T.; Stiers, E.; Botez, D.; Mawst, L.J. High power conversion efficiency Al-free diode lasers for pumping high power solid state laser systems. In Proceedings of the Conference on Novel In-Plane Semiconductor Lasers IV, San Jose, CA, USA, 24–27 January 2005.
30. Rattunde, M.; Mermelstein, C.; Schmitz, J.; Kiefer, R.; Pletschen, W.; Walther, M.; Wagner, J. Comprehensive modeling of the electro-optical-thermal behavior of (AlGaIn)(AsSb)-based 2.0 μm diode lasers. *Appl. Phys. Lett.* **2002**, *80*, 4085–4087. [[CrossRef](#)]
31. Qiao, Y.B.; Feng, S.W.; Xiong, C.; Zhu, H. Working Thermal Stresses in AlGaAs/GaAs High-Power Laser Diode Bars Using Infrared Thermography. *IEEE Trans. Device Mater. Reliab.* **2014**, *14*, 413–417. [[CrossRef](#)]
32. Piprek, J.; Abraham, P.; Bowers, J.E. Cavity length effects on internal loss and quantum efficiency of multi-quantum-well lasers. *IEEE J. Sel. Top. Quantum Electron.* **1999**, *5*, 643–647. [[CrossRef](#)]
33. Pankove, J.I. Temperature dependence of emission efficiency and lasing threshold in laser diodes. *IEEE J. Quantum Electron.* **1968**, *4*, 119–122. [[CrossRef](#)]

Disclaimer/Publisher’s Note: The statements, opinions and data contained in all publications are solely those of the individual author(s) and contributor(s) and not of MDPI and/or the editor(s). MDPI and/or the editor(s) disclaim responsibility for any injury to people or property resulting from any ideas, methods, instructions or products referred to in the content.